

# Electron transport in $\text{TiO}_2$ probed by THz time-domain spectroscopy

E. Hendry,<sup>1,\*</sup> F. Wang,<sup>2</sup> J. Shan,<sup>2</sup> T. F. Heinz,<sup>2</sup> and M. Bonn<sup>1,3</sup>

<sup>1</sup>*Leiden Institute of Chemistry, Leiden University, Einsteinweg 55, P.O. Box 9502, 2300 RA Leiden, The Netherlands*

<sup>2</sup>*Departments of Physics and Electrical Engineering, Columbia University, 538 West 120th Street, New York, New York 10027, USA*

<sup>3</sup>*FOM Institute for Atomic and Molecular Physics, Kruislaan 407, 1098 SJ, Amsterdam, The Netherlands*

(Received 1 December 2003; published 19 February 2004)

Electron transport in crystalline  $\text{TiO}_2$  (rutile phase) is investigated by frequency-dependent conductivity measurements using THz time-domain spectroscopy. Transport is limited by electron-phonon coupling, resulting in **a strongly temperature-dependent electron-optical phonon scattering rate, with significant anisotropy in the scattering process.** The experimental findings can be **described by Feynman polaron theory within the intermediate coupling regime and allow for a determination of electron mobility.**

DOI: 10.1103/PhysRevB.69.081101

PACS number(s): 72.40.+w, 71.38.-k, 72.10.Di, 72.20.Dp

Titanium dioxide ( $\text{TiO}_2$ ) is a wide-band-gap semiconductor with properties of both technological and fundamental interest. In addition to diverse industrial applications,  $\text{TiO}_2$  has recently gained importance for new photocatalysts and solar energy converters.<sup>1</sup> The characteristics of these devices, in which photogenerated carriers are used to trigger a chemical reaction or develop an electric potential, depend critically on the properties of charge transport. Indeed, for  $\text{TiO}_2$ -based dye-sensitized solar cells, it has been demonstrated that the efficiency is typically limited by electron transport through  $\text{TiO}_2$  nanostructures.<sup>1,2</sup> The issue of charge transport is also of considerable interest from the perspective of fundamental physics.  $\text{TiO}_2$ , an ionic transition-metal oxide, exhibits strong electron-phonon coupling, resulting in low room-temperature electron mobilities in the material.<sup>3–5</sup> However, despite its apparent importance, basic issues regarding charge transport in this material remain unclear. In particular, reported room-temperature electron Hall mobilities range from 0.01 to 10  $\text{cm}^2/\text{V s}$ .<sup>3–5</sup> In addition, the precise nature of the transport has remained unresolved. Because of the strong electron-phonon coupling in  $\text{TiO}_2$ , electrons are described in terms of polarons,<sup>6,7</sup> quasiparticles consisting of an electron and accompanying lattice deformation. For a sufficiently strong electron-phonon interaction, small polarons are formed. This corresponds to the limit of localized, self-trapped electrons, and charge transport typically occurs through thermally activated hopping from one site to the next. Large polarons, with spatially extended wave functions, are formed for weaker coupling strength. They exhibit band-type behavior, but with an enhanced mass relative to the band mass associated with an electron in a rigid lattice. Reports of the polaron mass in rutile range from  $8m_e$  to  $190m_e$  ( $m_e$  is the free electron mass),<sup>5,8–11</sup> and there have been conflicting arguments presented for the existence of small<sup>5,6,12</sup> and large<sup>9,13</sup> polarons in rutile. So although it is clear that the nature and efficiency of electron transport are determined by electron-phonon interactions that give rise to polaron formation and scattering events, the details of these interactions are unresolved.

In this Rapid Communication, we investigate electron-phonon interactions in single-crystal  $\text{TiO}_2$  samples by means of frequency-dependent conductivity measurements using THz time-domain spectroscopy (THz-TDS).<sup>14–16</sup> In addition

to providing critical information on the frequency dependence of the conductivity, from which scattering rates can be inferred directly, this all-optical approach eliminates the need for electrical contacts, which are often problematic with insulators. Furthermore, the photogeneration of charge carriers circumvents the possible complications associated with the required introduction of dopants or the use of nonstoichiometric compounds, typically involving oxygen deficiencies in  $\text{TiO}_2$ , which have been found to reduce mobility significantly.<sup>17</sup> The electron scattering rates obtained over a wide range of temperatures (10–300 K) can be explained by Feynman's polaron theory of the electron and its transport properties.<sup>18–21</sup> This nonperturbative treatment of the polaron is, unlike other formulations, not restricted to either limit of weak or strong electron-phonon coupling, bridging the region between large and small polarons. For  $\text{TiO}_2$ , we find intermediate-sized polarons with anisotropic mobilities of  $\sim 1 \text{ cm}^2/\text{V s}$ .

Rutile is the most common and stable  $\text{TiO}_2$  polymorph and has a tetragonal structure with  $a = 4.6 \text{ \AA}$  and  $c = 2.9 \text{ \AA}$ . While anatase-type  $\text{TiO}_2$  is more commonly used in solar cell devices,<sup>1</sup> rutile has been shown to behave very similarly in such devices.<sup>17,22,23</sup> The band gap of rutile is 2.9 eV at room temperature, increasing slightly at lower temperatures.<sup>24</sup> The 1-mm-thick single-crystal samples, grown commercially by Crystal-GmbH, are mounted in a helium cryostat. Crystals cut with (001) and (110) orientations provide the possibility to study the electronic response with the (THz) electric field perpendicular ( $\perp$ ) and parallel ( $\parallel$ ) to the  $c$  axis, respectively.

The experimental setup is similar to that described in Ref. 14. As shown in Fig. 1(a), THz pulses are essentially single cycle electromagnetic pulses, with a period of  $\sim 1 \text{ ps}$ . The field strength  $E(t)$  is detected directly in the time domain. We measure the transmission of these pulses through the unexcited sample  $[E(t)]$ , as well as through the irradiated sample  $[E_{\text{exc}}(t)]$ , in which electrons have been excited into the conduction band either by linear absorption (400 nm, 150 fs,  $4 \text{ J m}^{-2}$ ) or by two-photon absorption (800 nm, 150 fs,  $30 \text{ J m}^{-2}$ ). The fluence is kept sufficiently low to avoid effects from carrier-carrier interactions, which are observed for 400 nm fluences exceeding  $10 \text{ J m}^{-2}$ . Data analysis is most conveniently performed in the frequency domain using the corresponding Fourier transforms of the time domain data:  $E(\omega)$  and  $E_{\text{exc}}(\omega)$ . From these we can obtain the frequency-

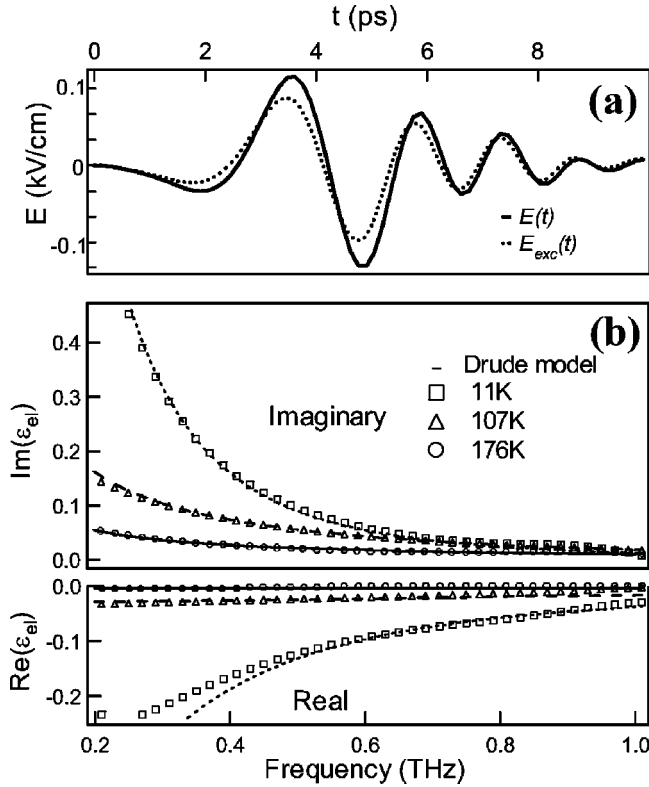


FIG. 1. (a) A pair of THz measurements at 10 K. The field strength transmitted through the unexcited sample [ $E(t)$ ] and the photoexcited sample [ $E_{exc}(t)$ ]. (b) Electronic contribution to the dielectric function of photoexcited rutile,  $\epsilon_{el}(\omega)$ , at temperatures of 11 K, 107 K, and 176 K, derived from the data in the upper panel. The experimental results are shown as symbols. The lines are fits to the Drude model, as discussed in the text. The data are measured for the THz field perpendicular to the  $c$  axis of rutile; similar behavior is observed for the THz field parallel to the  $c$  axis.

dependent electron dielectric function  $\epsilon_{el}(\omega, z)$  (Refs. 25 and 26) through the appropriate Fresnel equation:

$$\frac{E_{exc}(\omega)}{E(\omega)} = \frac{t_1[\epsilon_{lat}(\omega) + \epsilon_{el}(\omega, 0)]t_2[\epsilon_{lat} + \epsilon_{el}(\omega, L)]}{t_1[\epsilon_{lat}(\omega)]t_2[\epsilon_{lat}(\omega)]} \times \exp\left[i \frac{\omega}{2\sqrt{\epsilon_{lat}(\omega)}c} \langle \epsilon_{el}(\omega) \rangle L\right], \quad (1)$$

where  $L$  is the thickness of the sample and  $z$  the THz propagation coordinate. The Fresnel interface transmission factors  $t_1(\epsilon)$  and  $t_2(\epsilon)$  account for changes in reflective losses at the air-TiO<sub>2</sub>, and TiO<sub>2</sub>-air interfaces, respectively, and  $\langle \epsilon_{el}(\omega) \rangle = \int_0^L dz \epsilon_{el}(\omega, z)/L$  is the spatially averaged electronic dielectric function.  $\epsilon_{lat}(\omega)$  denotes the dielectric function of the unexcited rutile samples, associated with the lattice response, which is obtained for each temperature and crystal direction by comparing the THz transmission through rutile with that through air. The analysis is simplified by noting that the dominant effect of the induced response is in the exponential term. Since we measure the time-domain waveforms directly, we obtain the complete complex Fourier transforms (amplitude and phase) of the waveforms and can

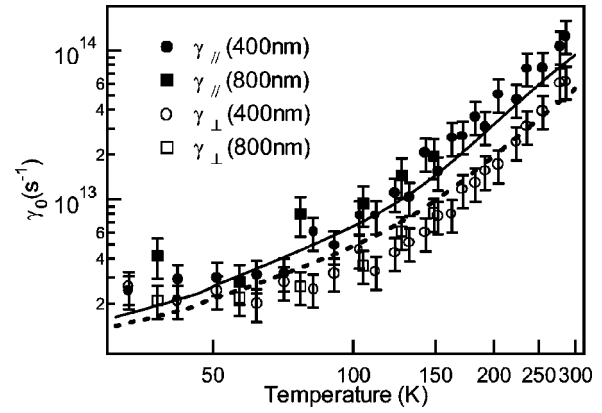


FIG. 2. Log-log plot of the inferred electron scattering rates in rutile for transport parallel to the  $c$  axis ( $\gamma_{||}$ , closed symbols) and perpendicular to the  $c$  axis ( $\gamma_{\perp}$ , open symbols), obtained with 400 and 800 nm excitation (circles and boxes, respectively). The lines are results of the Feynman polaron model described in the text with  $\alpha_{||} = 4$  (solid line) and  $\alpha_{\perp} = 6$  (dashed line).

thus deduce both the real and imaginary parts of  $\langle \epsilon_{el}(\omega) \rangle$  without further assumptions.<sup>14</sup> The dielectric function is directly related to the complex conductivity through  $\sigma_{el}(\omega) = i\omega\epsilon_{el}(\omega)$ .<sup>27</sup>

In Fig. 1(b),  $\langle \epsilon_{el}(\omega) \rangle$  is shown for three different temperatures. The frequency dependence of both the real and imaginary parts of the induced electronic response are compatible with the predictions of the Drude model for conductivity:<sup>27</sup>  $\epsilon_{el}(\omega) = -\omega_p^2/(\omega^2 + i\omega\gamma_0)$ . This simple model consists solely of two parameters: the electron plasma frequency  $\omega_p$  and the electron scattering rate  $\gamma_0$ . For the lower temperature range, these two parameters are uniquely determined by the fitting procedure. Above 150 K, the real part of  $\langle \epsilon_{el}(\omega) \rangle$ , corresponding to the pump-induced phase shift of the THz waveform, tends to zero with increasing temperature [Fig. 1(b)], as the carrier scattering rate  $\gamma_0$  becomes much larger than the probe frequencies. This complicates the direct extraction of both  $\gamma_0$  and  $\omega_p$ . However, the imaginary part of  $\langle \epsilon_{el}(\omega) \rangle$ , corresponding to the absorption of THz radiation by the conducting electrons, remains easily measurable. Hence, we can still deduce the scattering rate at higher temperatures by extrapolating the weakly temperature-dependent  $\omega_p$  to higher temperatures and using the imaginary part of  $\langle \epsilon_{el}(\omega) \rangle$  to determine  $\gamma_0$ .

As shown in Fig. 2, a very strong increase in the scattering rate  $\gamma_0$  is observed with increasing temperature. The anisotropy of charge transport is also clearly evident, with a significantly larger scattering rate measured for motion parallel to the  $c$  axis than perpendicular to it. We can describe the temperature dependence of  $\gamma_0$  in Fig. 2 by considering separate contributions from acoustic and optical phonons:

$$\gamma_0 = \gamma_{acoustic} + \gamma_{optical} = \beta T^{3/2} + \gamma_{optical}(\alpha, T). \quad (2)$$

The acoustic-phonon interaction—dominating at low temperatures—can be described by a  $\beta T^{3/2}$  temperature dependence, with  $\beta$  the strength of the acoustic-phonon-electron interaction.<sup>28</sup> The term  $\gamma_{optical}(\alpha, T)$  describes the

scattering from longitudinal optical (LO) phonons, which depends on the dimensionless electron-phonon coupling constant  $\alpha$  and temperature, and dominates at higher temperatures. In addition to its role in determining the scattering rate,  $\alpha$  is also the critical parameter describing polaron formation in the material. Thus an analysis of the temperature-dependent scattering rates in Fig. 2 should also shed light on the nature of polarons in TiO<sub>2</sub>.

The dominant LO phonon modes of TiO<sub>2</sub> can be inferred from infrared reflectivity data. For both crystal directions in rutile, modes with essentially identical frequencies of 24 THz (800 cm<sup>-1</sup>) dominate the spectra.<sup>9</sup> These modes are expected to play a dominant role in polaron formation and in scattering processes.

Although large ( $\alpha \ll 6$ ) and small ( $\alpha \gg 6$ ) polaron theories have been applied to describe polaron transport in TiO<sub>2</sub>,<sup>5,12,29</sup> it is clear that a reliable description of the temperature-dependent scattering rates requires a nonperturbative analysis, as embodied in the Feynman polaron theory.<sup>18–21</sup> Indeed, using this theory, we can reproduce our data with just two adjustable parameters:  $\beta$  (for the acoustic-phonon contribution) and  $\alpha$  (for the optical-phonon contribution). This fitting procedure involves minimizing Feynman's expression for the free energy of an electron,<sup>21</sup> including the interaction with the polar lattice, for each temperature and coupling constant. The analysis results in values of the electron-phonon coupling of  $\alpha_{\parallel} = 4.0 \pm 0.5$  and  $\alpha_{\perp} = 6.0 \pm 0.5$  for directions parallel and perpendicular to  $c$  axis, respectively (see Fig. 2). In determining the perpendicular coupling constant, which has two solutions in Feynman analysis, we made use of the constraint imposed by the band mass anisotropy:<sup>30</sup> stronger coupling is concomitant with higher electron band mass.<sup>7,21</sup> For both directions, the optical-phonon scattering dominates over the acoustic phonons, except at the lowest temperatures.

An interesting feature of the data is that the *higher* polaron scattering rate is observed for charge transport along the crystal direction for which a *higher* mobility has been previously reported.<sup>4,5</sup> This counterintuitive result can be understood by noting that the mobility ( $\mu$ ) is related to the scattering rate by  $\mu = e/(m^{**}\gamma_0)$ ,<sup>27</sup> so that the polaron mobility is determined not only by the scattering rate, but also by the polaron effective mass  $m^{**}$ . There are two factors contributing to a lower effective mass along the direction of strong scattering ( $c$  axis). The first is the anisotropy of the electron band mass, with *ab initio* predictions of the band mass yielding  $m_{\parallel}^* = 0.6m_e$  and  $m_{\perp}^* = 1.2m_e$ .<sup>30</sup> The more significant factor arises from a unique feature in Feynman theory: As shown in Fig. 3 for  $T = 300$  K, the calculated scattering rate as a function of  $\alpha$  exhibits a turning point at  $\alpha = 4$ , i.e., above  $\alpha = 4$  the scattering from optical phonons actually begins to *decrease* with increasing coupling strength. In contrast, the polaron mobility and radius are monotonically decreasing functions of the electron-phonon coupling strength. This situation arises because for  $\alpha > 4$  the polaron mass (see Fig. 3) tends rapidly towards the extremely large values associated with the small polaron regime.<sup>7</sup> For  $m_{\parallel}^* = 0.6m_e$  and  $m_{\perp}^* = 1.2m_e$ , the (room-temperature) polaron masses obtained from the Feynman

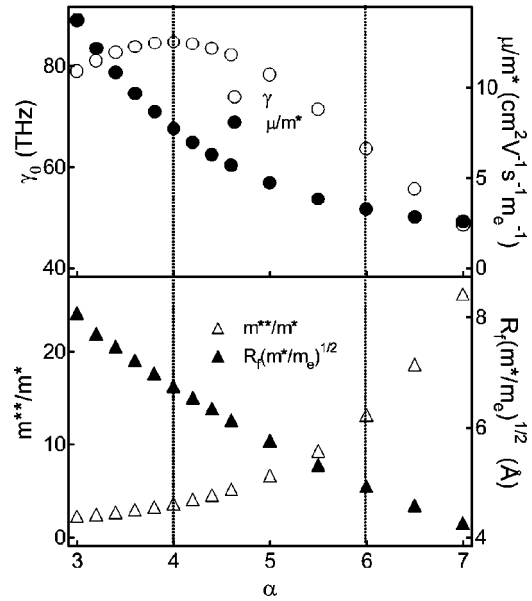


FIG. 3. Polaron scattering rate ( $\gamma_0$ ), with mobility ( $\mu$ ), mass ( $m^{**}$ ), and radius ( $R_f$ ), all normalized to the crystal band mass ( $m^*$ ), as a function of electron-phonon coupling strength  $\alpha$ , calculated using Feynman polaron theory (Refs. 18–21) for a phonon frequency of 24 THz, a temperature of 300 K, and  $\alpha$  between 3 and 7. In this range, while the polaron mobility is a monotonically decreasing function of  $\alpha$ , the polaron scattering rate exhibits a maximum at  $\alpha = 4$ . This region can be considered as a cross over from large to small polaron behavior, as indicated by the rapidly increasing effective mass  $m^{**}$  and decreasing polaron radius  $R_f$ . Dashed lines denote values relevant for this study.

model are  $m_{\parallel}^{**} = 2m_e$  and  $m_{\perp}^{**} = 15m_e$  for  $\alpha_{\parallel} = 4.0$  and  $\alpha_{\perp} = 6.0$ , respectively. Thus, the anisotropy in polaron mass is sufficiently large to counteract the anisotropy in the scattering rate. The derived room-temperature mobilities of  $\mu_{\parallel} = 8$  cm<sup>2</sup>/V s and  $\mu_{\perp} = 1.4$  cm<sup>2</sup>/V s reproduce the anisotropy of recent Hall measurements and are of comparable magnitude.<sup>5</sup>

The polaron radius—the spatial extent of the electronic wave function—determined by the electron-phonon coupling constant, is calculated following Schultz<sup>20</sup> and plotted in Fig. 3. Clearly, it is comparable to the lattice spacing ( $a = 4.6$  Å and  $c = 2.9$  Å). The intermediate size of the polaron may account for some of the conflicting conclusions drawn previously in studies of transport in rutile.<sup>5,6,9,12,13</sup> With respect to solar cell applications using nanoparticles, the small mean free paths (from the large scattering rates) and small polaron size demonstrate that scattering at room temperature is dominated by bulk TiO<sub>2</sub> properties, since these are orders of magnitude smaller than the typical  $\sim 25$  nm radius of particles used for such applications. Surface scattering effects observed in individual TiO<sub>2</sub> particles at low temperatures<sup>16</sup> (77 K) will be negligible at room temperature. However, the much lower reported room-temperature mobilities of photo-generated carriers in *bulk porous* rutile<sup>23</sup> ( $< 10^{-3}$  cm<sup>2</sup>/V s, as opposed to  $\sim 1$  cm<sup>2</sup>/V s reported here) indicate that charge transport in solar cells is not limited by electron-phonon in-

teractions, but by the transport across the interfaces of different crystalline regions. The mobility observed here ( $\sim 1 \text{ cm}^2/\text{Vs}$ ) represents the intrinsic limit for electron transport at room temperature in  $\text{TiO}_2$ . Our results demonstrate that substantial device improvement is possible if interfacial effects can be eliminated.

The authors are greatly indebted to Professor J. R. Chelikowsky for supplying detailed data on the calculated band structure of  $\text{TiO}_2$  for a determination of the electron and hole

band mass, B. O'Regan, P.C.M. Planken, G.J. Kroes, and A.W. Kleyn for many helpful discussions, and R.C.V. van Schie and P. Schakel for their excellent technical support. This work is part of the research program of the Stichting voor Fundamenteel Onderzoek der Materie (FOM), which is financially supported by the Nederlandse organisatie voor Wetenschappelijk Onderzoek (NWO). The US portion of this work was supported primarily by the MRSEC Program of the NSF under Grant No. DMR-0213574.

\*Electronic address: e.hendry@chem.leidenuniv.nl

- <sup>1</sup>K. Kalyanasundaram and M. Gratzel, *Coord. Chem. Rev.* **177**, 347 (1998).
- <sup>2</sup>N. Kopidakis, E. A. Schiff, N. G. Park, J. v. d. Lagemaat, and A. J. Frank, *J. Phys. Chem. B* **104**, 3930 (2000).
- <sup>3</sup>R. G. Beckenridge and W. R. Hosler, *Phys. Rev.* **91**, 793 (1953).
- <sup>4</sup>V. N. Bogomolov and V. P. Zhuze, *Sov. Phys. Solid State* **5**, 2404 (1964).
- <sup>5</sup>E. Yagi, R. R. Hasiguti, and M. Aono, *Phys. Rev. B* **54**, 7945 (1996).
- <sup>6</sup>A. S. Alexandrov and N. Mott, in *Polarons and Bipolarons* (World Scientific, Singapore, 1995), pp. 155–157.
- <sup>7</sup>D. Emin, *Phys. Rev. B* **48**, 13 691 (1993).
- <sup>8</sup>W. R. Thurber and A. J. H. Mante, *Phys. Rev.* **139**, A1655 (1962).
- <sup>9</sup>J. F. Baumard and F. Gervais, *Phys. Rev. B* **15**, 2316 (1977).
- <sup>10</sup>J. W. DeFord and O. W. Johnson, *J. Appl. Phys.* **54**, 889 (1983).
- <sup>11</sup>T. R. Sandin and P. H. Keeson, *Phys. Rev.* **177**, 1370 (1969).
- <sup>12</sup>V. N. Bogomolov, E. K. Kudinov, Yu, and A. Firsov, *Sov. Phys. Solid State* **9**, 2502 (1968).
- <sup>13</sup>A. E. Myasnikova, *Phys. Lett. A* **291**, 439 (2001).
- <sup>14</sup>M. C. Beard, G. M. Turner, and C. A. Schmittenmaer, *J. Phys. Chem. B* **106**, 7146 (2002).
- <sup>15</sup>J. Shan, F. Wang, E. Knoesel, M. Bonn, and T. F. Heinz, *Phys. Rev. Lett.* **90**, 247401 (2003).
- <sup>16</sup>G. M. Turner, M. C. Beard, and C. A. Schmittenmaer, *J. Phys. Chem. B* **106**, 11716 (2002).
- <sup>17</sup>S. Fu and T. Egami, *Proc. SPIE* **2697**, 520 (1996).
- <sup>18</sup>R. P. Feynman, *Phys. Rev.* **97**, 660 (1955).
- <sup>19</sup>R. P. Feynman, R. W. Hellwarth, C. K. Iddings, and P. M. Platzman, *Phys. Rev.* **127**, 1004 (1962).
- <sup>20</sup>T. D. Schultz, *Phys. Rev.* **116**, 526 (1959).
- <sup>21</sup>R. W. Hellwarth and I. Biaggio, *Phys. Rev. B* **60**, 299 (1999).
- <sup>22</sup>N. G. Park, J. v. d. Lagemaat, and A. J. Frank, *J. Phys. Chem. B* **104**, 8989 (2000).
- <sup>23</sup>T. Dittrich, *Phys. Status Solidi A* **182**, 447 (2000).
- <sup>24</sup>H. Tang, F. Levy, H. Berger, and P. E. Schmid, *Phys. Rev. B* **52**, 7771 (1995).
- <sup>25</sup>C. W. Chu, *Phys. Rev. B* **1**, 4700 (1970).
- <sup>26</sup>By comparing the transmission of photoexcited  $\text{TiO}_2$  to transmission experiments on a reduced sample ( $n$ -type doped  $\text{TiO}_{2-x}$ ,  $x \sim 0.0005$ ), we conclude that the pump-induced THz absorption originates primarily from the photogenerated electrons, rather than from holes. This is in accordance with the large hole band mass ( $> 4m_e$ , Ref. 27) and resulting large (small) polaron mass (mobility).
- <sup>27</sup>N. W. Ashcroft and N. D. Mermin, in *Solid State Physics* (Saunders College, 1976), pp. 16, 17, 323, 519, 601.
- <sup>28</sup>J. Bardeen and W. Shockley, *Phys. Rev.* **80**, 72 (1950).
- <sup>29</sup>F. E. Low and D. Pines, *Phys. Rev.* **98**, 414 (1955).
- <sup>30</sup>K. M. Glassford and J. R. Chelikowsky, *Phys. Rev. B* **46**, 1284 (1992).